Modelling and characterising the Point Spread Function in astronomical images with PSFEx

E. Bertin[1], Ph. Delorme[2], A.Baillard[1], C.Marmo[1] and G. Sémah[1]

[1] Institut d'Astrophysique de Paris (IAP), 98bis, bd Arago, F-75014 Paris, France
   e-mail: `bertin@iap.fr`
[2] Laboratoire d'Astrophysique de Grenoble, BP 53X, F-38041 Grenoble Cedex, France,
   e-mail: `Philippe.Delorme@obs.ujf-grenoble.fr` *

ABSTRACT

Context. Deriving the Point Spread Function (PSF) of an astronomical image is a required step in tasks such as crowded field photometry, star/galaxy separation, galaxy morphology, as well as image quality control.
Aims. We present the techniques implemented in PSFEx, a companion program to the SExtractor (Bertin & Arnouts 1996) source extraction package, to extract, model and characterise the PSF of astronomical images in a robust and fully automated way.
Methods. We show how PSFEx can recover variable PSFs of arbitrary shapes from undersampled data, using decompositions on an appropriate set of basis vectors.
Results. Results on images coming from simulations as well as mosaic cameras such as MEGACAM and WIRCam are presented.
Conclusions. PSFEx is released to the community under the CeCILL Public Licence.

Key words. data analysis – image processing – point spread function

1. Introduction

The flux response of modern imaging devices is close to linear over a large dynamic range and translation-invariant to a good approximation within the observed field of view. Hence for such devices a Point Spread Function (PSF) can be derived that defines much of their instrumental performance (besides noise properties). In Astronomy, knowing the PSF is key to many scientific analysis tasks such as detection (matched filtering over stationary background noise), star/galaxy separation, galaxy morphology, weak shear analysis or differential photometry. In large sky surveys, which can comprise millions of exposures, the PSF and its variations can be used in quality control procedures to detect efficiently instrumental problems such as defocused or abnormally aberrated exposures, exceedingly bad atmospheric conditions and guiding errors.

The PSFEx (for PSF EXtraction) software tool was written as a companion program to the SExtractor source extraction package (Bertin & Arnouts 1996), with the purpose of providing a universal PSF modelling and measurement tool. The PSFEx prototype has been developed over many years and has already been used in several stellar studies relying on PSF-fitting photometry (e.g. Kalirai et al. 2001a,2001b, Moraux et al. 2003,

Kendall et al. 2005, Lodieu et al. 2006, Delorme et al. 2008), as well as galaxy morphology (Bertin et al., in preparation).

This article describes all the steps followed by PSFEx for modelling and characterising the PSF. First, in §2 and §3 we introduce our approach to modelling the PSF profile and its variations. In §4 we present our recipe for identifying point-sources suitable as realisations of the local Point Spread Function. In §5 we propose some metrics for measuring image quality based on the PSF. Finally we comment our results and point out possible improvements in §8.

2. Modelling

For astronomers, the most important parameter characterising the PSF is the Full-Width-at-Half-Maximum (FWHM) of the main PSF lobe, expressed in arc seconds. The smaller the FWHM, the sharper the images. Without adaptive optics, on ground-based telescopes with apertures $\gg 10\,\text{cm}$, the PSF FWHM is dominated by the contribution from atmospheric turbulence, the so-called *seeing*. In such conditions, for long exposures ($> 1\,\text{s}$) the angular Modulation Transfer Function (MTF) is well represented by $\exp(-\omega/\omega_c)^{-5/3}$ as expected from a Kolmogorov turbulence model, with $\omega_c \approx 2.921/\text{FWHM}$ (e.g. Roddier 1981, Racine 1996). There is no simple analytical expression in real space corresponding to this MTF, however the core is close to Gaussian, and the profile is well fitted by a Moffat (1969) function (Trujillo et al. 2001).

Analytical functions such as Moffats, Lorentzians or Gaussian mixtures have been used with success to model the PSF of ground-based instruments (Franz 1973, Penny 1979, Buonanno et al. 1983, Gilliland & Brown 1987, Schechter et al. 1993). They can also provide a satisfactory match to undersampled data (FWHM ≲ 2.5 pixels) after the functions have

been convolved with the intra-pixel response function (Stetson 1987, Buonanno & Iannicola 1989, Penny & Leese 1996). Unfortunately the analytical functions above are poor approximations of diffraction-limited PSFs, or PSFs dominated by optical aberrations, as in the corners of wide-field instruments. To circumvent this limitation, analytical models can be supplemented with pixel lookup tables, that is, PSF image components tabulated at low resolution (e.g., Stetson 1987). These combinations have the big disadvantage that they cannot reproduced peripheral features commonly aliased like diffraction rings or spikes. Moreover, even when the central peak of the undersampled PSF has a smooth and even profile, the intra-pixel response function may be much bumpier than the assumed door function (e.g. Lauer 1999b, Toyozumi 2006, Barron et al. 2007) and charge diffusion is often the leading factor (e.g. Krist 2004).

As an alternative, PSFs may also be modelled as linear combinations of the appropriate basis functions. The optical point spread function of an instrument being the Fourier Transform of the auto-correlation of its pupil, the PSF of any instrument with a finite aperture is bandwidth-limited. According to the Shannon sampling theorem it can therefore be perfectly reconstructed (interpolated) from an infinite table of regularly-spaced samples. For a finite table the reconstruction will not be perfect: extended features, such as profile wings and diffraction spikes caused by the high frequency component of the pupil function, will obviously be cropped. With this limitation in mind, one may nevertheless reconstruct with good accuracy a tabulated PSF thanks to sinc interpolation (e.g. Lupton & Gunn 1986). Undersampled PSFs can also be represented in the form of tabulated data provided that a finer grid satisfying Nyquist's criterion is used (Anderson & King 2000, Mighell 2005).

For reasons of flexibility and interoperability with other software, we chose to represent PSFs in PSFEx as small images with adjustable resolution. These PSF "images" can be either derived directly, treating each pixel as a free parameter ("pixel" vector basis), or more generally as a combination of basis vector images.

2.1. Pixel basis

2.1.1. Recovering aliased PSFs

If the data are undersampled, unaliased Fourier components can in principle be recovered from the images of several point-sources randomly located with respect to the pixel grid, using the principle of super-resolution (Huang & Tsai 1984). Let $\Phi(u, v)$ be the Fourier transform of the PSF, $(\Delta x_s, \Delta y_s)$ the fractional part of the vector shift of point-source s with respect to the pixel grid, and A_s its total flux. Assuming that the signal total bandwidth is comprised between 1 and 2 per pixel, the Fourier transform of the aliased image of point-source s, $F_s(u, v)$, obeys the relation

$$
\begin{aligned}
F_s(u, v) = A_s.e^{ux_s+vy_s} \quad &(\Phi(u, v) \\
&+e^{-2i\pi\Delta x_s}\Phi(u - 1, v) \\
&+e^{-2i\pi\Delta y_s}\Phi(u, v - 1) \\
&+e^{-2i\pi(\Delta x_s+\Delta y_s)}\Phi(u - 1, v - 1)).
\end{aligned} \quad (1)
$$

In that case a minimum of 4 point-sources is necessary to recover the unaliased Fourier components $\Phi(u, v)$. More severe undersampling would require more sources, but this is unlikely to happen as FWHMs much below 1 pixel are unusual for instrumental PSFs: for most imagers, the MTF of the intra-pixel response (especially charge diffusion) strongly dampens Fourier components with spatial wavelengths below the pixel size.

Working in the Fourier domain using the method above, Lauer (1999a) shows how PSFs from the Hubble Space Telescope Planetary Camera and Wide-Field Planetary Camera can be reconstructed at 3 times the original instrumental sampling from a large number of undersampled star images. However solving (1) in the Fourier domain gives far from satisfactory results with real data. Images have boundaries; the wings of point-source profiles may be contaminated with artifacts or background sources; the noise process is far from stationary behind point-sources with high S/N, because of the local photon-noise contribution from the sources themselves. All these features generate spurious Fourier modes in the solution, which appear as parasitic ripples in the final, super-resolved PSF.

A more robust solution is to work directly in pixel space, using an interpolation function; we may use the same interpolation function later on to *fit* the tabulated PSF model for point-source photometry. Let $\boldsymbol{\phi}$ be the vector representing the tabulated PSF, $h_s(\boldsymbol{x})$ an interpolation function, and η the original image sampling step to PSF sampling step ratio (oversampling factor). The interpolated value at image pixel i of $\boldsymbol{\phi}$ centered on coordinates $\boldsymbol{x}_s$ writes

$$
\phi'_i(\boldsymbol{x}_s) = \sum_j h_s\left(\boldsymbol{x}_j - \eta.(\boldsymbol{x}_i - \boldsymbol{x}_s)\right)\phi_j \quad (2)
$$

Note that η can be less than 1 in the case where the image is generously sampled. Using multiple point sources s sharing the same PSF, but centred on various coordinates $\boldsymbol{x}_s$, and neglecting the correlation of noise between pixels, we can derive the components of ϕ that provide the best fit (in the least-square sense) to the point-source images by minimising the cost function:

$$
E(\boldsymbol{\phi}) = \chi^2(\boldsymbol{\phi}) = \sum_s \sum_{i\in\mathcal{D}_s} \frac{\left(p_i - f_s\phi'_i(\boldsymbol{x}_s)\right)^2}{\sigma_i^2}, \quad (3)
$$

where f_s is the integrated flux of point-source s, p_i the number of counts (ADUs) recorded above the background at image pixel i, and $\mathcal{D}_s$ the set of pixels around s. In the variance estimate of pixel i, σ_i^2, we identify three contributions:

$$
\sigma_i^2 = \sigma_b^2 + \frac{p_i}{g} + (\alpha.p_i)^2. \quad (4)
$$

σ_b^2 is the pixel variance of the local background. p_i/g, where g is the detector gain in e^-/ADU, is the variance contributed by photons from the source itself. The third term in (4) will generally be negligible except for high p_i values; the α factor accounts for pixel-to-pixel uncertainties in the flat-fielding, variation of the intra-pixel response function, and apparent fluctuations of the PSF due to interleaved "micro-dithered" observations[1] or lossy image resampling. Depending on image quality, suitable values for α will range from less than one thousandth to a few percents.

f_s is measured by integrating the flux in a defined aperture. This aperture will define the normalisation of the PSF. Its diameter must be sufficient to prevent the measurement to be too sensitive to centering or pixellation effects, but not excessively large to avoid too strong S/N degradation and contamination by neighbours. In practice, a $\approx 5''$ diameter provides a fair compromise with good seeing images (PSF FWHM $< 1.2''$),

---

[1] Micro-dithering consists of observing n^2 times the same field with repeated $1/n$ pixel shifts in each direction to provide properly sampled images despite using large pixels. Although the observed frames can in principle be recombined with an "interleaving" reconstruction procedure, changes in image quality from exposure to exposure may often lead to jaggies along gradients of source profiles, as can sometimes be noticed in DeNIS or WFCAM images.
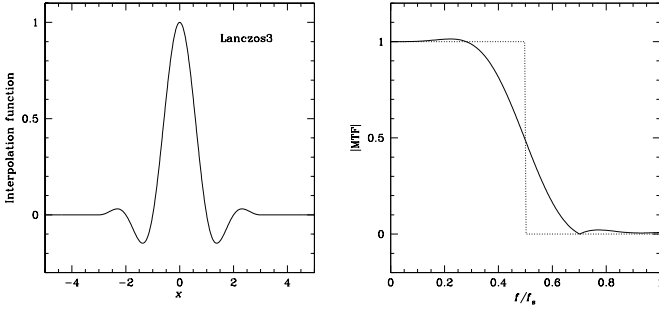
Fig. 1. The Lánczos3 interpolant in one dimension (*left*), and its modulation transfer function (*right*).

2.1.2. Interpolating the PSF model

As we saw, one of the main interests of interpolating the PSF model in direct space is that it involves only a limited number of PSF "pixels". However, as in any image resampling task, a compromise must be found between the perfect Shannon interpolant (unbounded sinc function), and simple schemes with excessive smoothing and/or aliasing properties like bi-linear interpolation ("tent" function) (see Wolberg 1992). Experimenting with the SWARP image resampling prototype (Bertin et al. 2002), we found in the Lánczos3 interpolant (Fig. 1) a reasonable compromise: the kernel footprint is 6 PSF pixels in each dimension, and the modulation transfer function is close to flat up to $\approx 60\%$ of the Nyquist frequency.

A typical minimum of 2 to 2.5 pixels per PSF Full-Width at Half-Maximum (FWHM) is required to sample an astronomical image without generating significant aliasing (see Bernstein 2002). Consequently, we adopt a default sampling step for the PSF model corresponding to 4 model "pixels" per PSF FWHM.

2.1.3. Regularisation

For $\eta \gg 1$, the system of equations obtained from minimising (3) becomes ill-conditioned and requires regularisation (Pinheiro da Silva 2006). Our experience with PSFEx shows that the solutions obtained over the domain of interest for astronomical imaging ($\eta \lesssim 3$) are robust in practice, and that regularisation is generally not needed. However, it may happen, especially with infrared detectors, that samples of undersampled point-sources are contaminated by image artifacts; and solutions computed with (3) become unstable. We therefore added a simple Tikhonov regularisation scheme to the cost function:

$$E(\boldsymbol{\phi}) = \chi^2(\boldsymbol{\phi}) + \|\mathbf{T}\boldsymbol{\phi}\|^2. \tag{5}$$

In image processing problems the (linear) Tikhonov operator $\mathbf{T}$ is usually chosen to be a high-pass filter to favour "smooth" solutions. PSFEx adopts a slightly different approach by reducing $\mathbf{T}$ to a scalar weight $1/\sigma_\phi^2$ and performing a procedure in two steps.

1. PSFEx makes a first rough estimate of the PSF by simply shifting point-sources to a common grid and computing a median image $\boldsymbol{\phi}^{(0)}$. With undersampled data this image represents a smooth version of the real PSF.

2. Instead of fitting directly the model to pixel values, PSFEx fits the difference $\Delta\phi$ between the model and $\boldsymbol{\phi}^{(0)}$. $E(\boldsymbol{\phi})$ becomes

$$E(\boldsymbol{\phi}) = \sum_s \sum_{i \in \mathcal{D}_s} \frac{\left(p_i - f_s\left((\phi_i'^{(0)}(\boldsymbol{x}_s) + \Delta\phi_i'(\boldsymbol{x}_s))\right)\right)^2}{\sigma_i^2} + \sum_j \frac{\Delta\phi_j^2}{\sigma_\phi^2}. \tag{6}$$

Minimising (6) with respect to the $\Delta\phi_j$'s comes down to solving the system of equations

$$
\begin{aligned}
0 &= \frac{\partial E}{\partial \Delta\phi_k} \\
&= 2f_s \sum_s \sum_{i \in \mathcal{D}_s} \frac{1}{\sigma_i^2} h_s\left(\boldsymbol{x}_k - \eta.(\boldsymbol{x}_i - \boldsymbol{x}_s)\right) \\
&\quad \times \left(f_s \sum_j h_s\left(\boldsymbol{x}_j - \eta.(\boldsymbol{x}_i - \boldsymbol{x}_s)\right)(\phi_j^{(0)} + \Delta\phi_j) - p_i\right) \\
&\quad + \frac{2}{\sigma_\phi^2} \Delta\phi_k.
\end{aligned}
\tag{7}
$$

In practice the solution appears to be fairly insensitive to the exact value of σ_ϕ except with low signal-to-noise conditions or contamination by artifacts. $\sigma_\phi \approx 10^{-2}$ seems to provide a good compromise by bringing efficient control of noisy cases but no detectable smoothing of PSFs with good data and high signal-to-noise.

The system in (7) is solved by PSFEx in a single pass. Much of the processing time is actually spent in filling the normal equation matrix, which would be prohibitive for large PSFs if the sparsity of the design matrix were not put to contribution to speed up computations.

2.2. Shapelet basis

Two-dimensional Gauss-Hermite functions provide another convenient orthonormal basis for representing local image features. The basis vectors are

$$\psi_{n_1,n_2}(\boldsymbol{x}) = \frac{1}{\sigma \sqrt{2^{n_1+n_2} n_1! n_2!}} H_{n_1}\left(\frac{x_1}{\sigma}\right) H_{n_2}\left(\frac{x_2}{\sigma}\right) e^{-|\boldsymbol{x}|^2/2\sigma^2}, \tag{8}$$

where $H_n(x)$ is a Hermite polynomial of order n, and σ a scaling factor. Gauss-Hermite functions were originally introduced in the image processing community to provide a mathematical model of the receptive fields in the early stage of mammalian spatial vision (Martens 1990), and later used for such diverse applications as feature extraction, image compression and indexing, or artifact removal (see e.g. Martens 2006 for a review).

In the field of astronomical imaging, where they were popularised under the name of *shapelets*, they have proven to be quite effective at describing PSF variations for differential photometry and PSF ellipticities for weak lensing applications (Alard & Lupton 1998, Bernstein & Jarvis 2002, Refregier 2003).
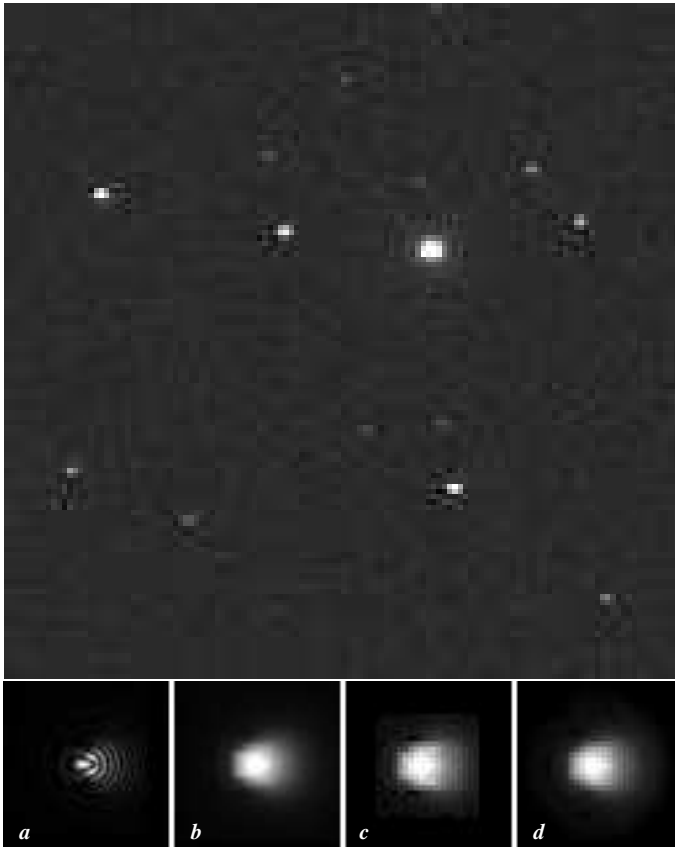
The *polar* version of shapelets (Massey & Refregier 2005) provides a more "natural" orthonormal basis for broadly circular profiles

$$\psi_{n,m}(r,\theta) = \frac{(-1)^{\frac{n-|m|}{2}}}{\sigma} \sqrt{\frac{\frac{n-|m|}{2}!}{\pi \frac{n+|m|}{2}!}} L_{\frac{n-|m|}{2}}^{(|m|)}\left(\frac{r^2}{\sigma^2}\right) \times \left(\frac{r}{\sigma}\right)^{|m|} e^{-\frac{1}{2}\left(\frac{r}{\sigma}\right)^2 - im\theta}, \tag{9}$$

where $(n - |m|)/2 \in \mathbb{N}$ and $L_n^{(\alpha)}(x)$ is the associated Laguerre polynomial

$$L_n^{(\alpha)}(x) = \frac{1}{n!} x^{-\alpha} e^x \frac{d^n}{dx^n}\left(x^{n+\alpha} e^{-x}\right) \tag{10}$$

$$= \sum_{k=0}^n \frac{(\alpha + n)!}{k!(n-k)!(\alpha + k)!} (-x)^k. \tag{11}$$

Fig. 2. Example of an extreme case of PSF recovery. *Top*: part of a simulated star field image with strong undersampling. *Bottom, from left to right*: (a) simulated optical PSF, (b) simulated PSF convolved by the pixel response, (c) PSF recovered by PSFEx at 4.5 times the image resolution from a random sample of 212 stars extracted in the simulated field above, using the "pixel" vector basis (§2.1), and (d) PSF recovered using the "shapelet" basis (§2.2) with $n_{\max} = 16$.

The number of shapelet vectors with $n \leq n_{\max}$ is

$$N_{\max} = (n_{\max} + 1)(n_{\max} + 2)/2. \qquad (12)$$

Shapelet decompositions with finite $n \leq n_{\max}$ are only able to probe a restricted range of scales. Refregier (2003) quotes $r_{\min} = \sigma/\sqrt{n_{\max} + 1}$ and $r_{\max} = \sigma\sqrt{n_{\max} + 1}$ as the standard deviation of the central lobe and the whole shapelet profile, respectively. In practice, the diameter of the circle enclosing the region where images can be fitted with shapelets is only about $\approx 2.5 r_{\max}$. Hence modelling accurately both the wings and the core of PSFs with a unique set of shapelets requires a very large number of shapelet vectors, typically several hundreds.

3. Managing PSF variations

3.1. Basic formalism

Few imaging systems have a perfectly stable PSF, be it in time or position; for most instruments the approximation of a constant PSF is valid only on a small portion of an image at a time. Position-dependent variations of the PSF on the focal plane are generally caused by optics, and exhibit a smooth behaviour which can be modelled with a low-order polynomial.

The most intuitive way to generate variations of the PSF model is to apply some warping to it (enlargement, elongation, skewness, ...). But this description is not appropriate with PSFEx

because of the non-linear dependency of PSF vector components towards warping parameters. Instead, we can extend the formalism of (6) by describing the PSF as a variable, linear combination of PSF vectors $\boldsymbol{\phi}_c$; each of them associated to a basis function X_c of some parameter vector $\boldsymbol{a}$ like image coordinates:

$$E(\boldsymbol{\phi}) = \sum_s \sum_{i \in \mathcal{D}_s} \frac{\left(p_i - f_s \sum_c X_c(\boldsymbol{a})\left((\phi'^{(0)}_{c\,i}(\boldsymbol{x}_s) + \Delta\phi'_{c\,i}(\boldsymbol{x}_s))\right)\right)^2}{\sigma_i^2}$$
$$+ \sum_j \sum_c \frac{\Delta\phi^2_{c\,j}}{\sigma^2_\phi}. \qquad (13)$$

The basis functions X_c in the current version of PSFEx are limited to simple polynomials of the components of $\boldsymbol{a}$. Each of these components a_l belongs to a "distortion group" $g = 0, 1, ..., N_g$, such that

$$X_c(\boldsymbol{a}) = \prod_{g < N_g} \left(\prod_{(\sum_{l \in \Lambda_g} d_l) \leq D_g} a_l^{d_l} \right), \qquad (14)$$

where Λ_g is the set of parameter indices l that concern the distortion group g, and $D_g \in \mathbb{N}$ is the polynomial degree of group g. The product runs over all compatible combinations of $d_l \in \mathbb{N}$ and g. The polynomial engine of PSFEx is the same as the one implemented in the SCAMP software (Bertin 2005) and can use any set of SExtractor and/or FITS header parameters as components of $\boldsymbol{a}$. Although PSF variations are more likely to depend essentially on source position on the focal plane, it is thus possible to include explicit dependency on parameters such as telescope position, time, or source flux (Fig. 4). In practice, a third-degree polynomial on pixel coordinates (represented by 20 PSF vectors) is able to map PSF variations with good accuracy on most images (Fig. 3).

3.2.

Accurate modelling of the PSF with the scheme described above involves a fairly large number of degrees of freedom, and is therefore somewhat sensitive to noise in the point-source sample. This is especially notable in exposures with a small number of point sources, and/or where the PSF exhibits strong variations over the field of view. Hopefully, one can drastically reduce the number of degrees of freedom necessary to provide a good description of the PSF and its variations by using a vector basis better suited to a specific instrument than the "generic" pixel and shapelet bases described in §2.1 and §2.2.

It is easy to show (e.g. Theodoridis & Koutroumbas 2003) that Principal Component Analysis (PCA) provides the basis which requires the lowest number of vectors to approximate a set of data (images) within a given Mean Square Error, assuming the noise is additive and uncorrelated between images. PCA has already been proposed and used by several authors (Lupton et al. 2001, Jee et al. 2007) to represent the PSF and its variations. In these studies, the PCA is directly applied to a selection of point-source images which have been re-centred by resampling. There are however some major drawbacks with this approach. (1) It requires well-sampled images. (2) Because of the vast range of fluxes found among field stars, linear combinations derived from the PCA are sub-optimum in terms of signal-to-noise (unless a weighted PCA scheme is used). (3) PCA relies on 2nd order statistics and is therefore particularly sensitive to contamination from outliers. With the "direct" approach above, the
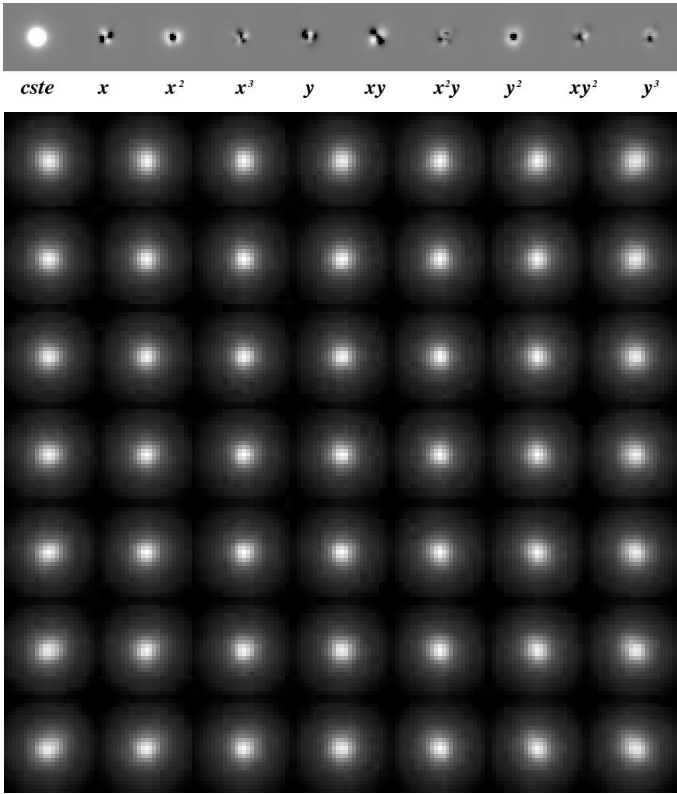
Fig. 3. Example of PSF mapping as a function of pixel coordinates in PSFEx. *Top*: PSF component vectors for each polynomial term derived from the CFHTLS-deep "D4" r-band stack observed with the MEGACAM camera. A third-degree polynomial was chosen for this example. Note the prominent variation of PSF width with the square of the distance to the field centre. *Bottom*: reconstruction of the PSF over the field of view (the grey scale has been slightly compressed to improve clarity).
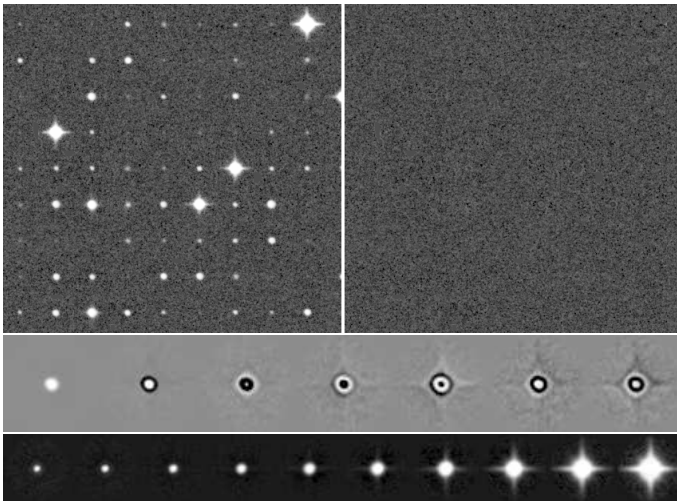
Fig. 4. Example of PSF mapping on images from a non-linear imaging device. 1670 point-sources from the central 4096×4096 pixels of a photographic density scan (SERC J #418 survey plate, courtesy of J. Guibert, CAI, Paris observatory) were extracted using SEXTRACTOR, and their images run through PSFEx. A sample is shown at the *top-left*. The PSF model was given a 6th degree polynomial dependency on the instrumental magnitude measured by SEXTRACTOR (MAG_AUTO). *Middle*: PSF components derived by PSFEx. *Bottom*: reconstructed PSF images as a function of decreasing magnitude. *Top-right*: sample residuals after subtraction of the PSF-model.

relative contribution from the various detections to the Principal Components is not tight to any parameter on which the PSF is supposed to depend, like image coordinates (i.e. some artifact in the centre of a frame contributes as much as an isolated, "genuinely distorted" point-source in the corner): outliers are difficult to filter out.

For all these reasons, the application of PCA in PSFEx is not done directly on the data, but on model images from several exposures, reconstructed from the ϕ_c's derived in (13).

4. Selecting point-sources

Extracting the PSF from an astronomical image is much easier than from an "everyday life" picture (see, e.g. Luxen & Förstner 2002, Hall & Qiu 2007 and references therein), thanks to the presence of unresolved sources (stars or quasars) over the field of view. Nevertheless, in some astronomical observations, the fraction of suitable point sources that may be used as good approximations to the local PSF may be rather low. This is especially true for deep imaging in the vicinity of galaxy clusters at high galactic latitudes, where unsaturated stars may comprise only a small percentage of all detectable sources. In our wish to minimise as much as possible assumptions about the shape of the PSF, we are left with the following selection criteria:

- the shape of suitable unresolved (unsaturated) sources does not depend on the flux.
- amongst the image profiles of all real sources, those from unresolved sources have the smallest FWHM.

These considerations and experimentation led us to adopt as a starting point to selection a procedure similar to the rectangular cut in the half-light-radius (r_{h}) vs magnitude plane popular amongst member of the weak lensing community (Kaiser et al. 1995). r_{h} is well estimated by SEXTRACTOR's FLUX_RADIUS parameter. In PSFEx the "vertical" locus produced by point sources (whose shape does not depend on magnitude) is automatically framed between a minimum signal-to-noise threshold and the saturation limit on the magnitude axis, and within some margin around the local mode on the r_{h} axis (Fig. 5). Additionally, to provide a better rejection of image artifacts and multiple objects, PSFEx excludes detections flagged by SEXTRACTOR as blended or cropped and those with aspect ratios higher than some predefined limit (typically 2:1).

Despite the filtering process, a small fraction of the remaining point-sources candidates (typically 5-10% on ground-based optical images at high galactic latitude) is still unsuitable to serve as a realisation of the local PSF, because of contamination by neighbour objects. Iterative procedures to subtract the contribution from neighbour stars have been successfully applied in crowded fields (Stetson 1987, Magain et al. 2007). However these techniques do not solve the problem of pollution by non-stellar objects like image artefacts, a common curse of wide field imaging, and contaminated point-sources still have to be filtered out. The rejection process at play in PSFEx works by deriving a first PSF model estimate, and computing a map of residuals from the fit by this model for each point-source (Fig. 6): each pixel of the map is the square of the difference square of the model with the data, divided by the σ_i^2 estimate from (4). The PSF model may still be "rough" at this stage, hence to avoid penalising poorly fitted bright source pixels, the factor α is initially set to a fairly large value, 0.1-0.3. Assuming that the fitting errors are normally distributed, and given the large number of degrees of freedom (the tabulated values of the model), the distribution
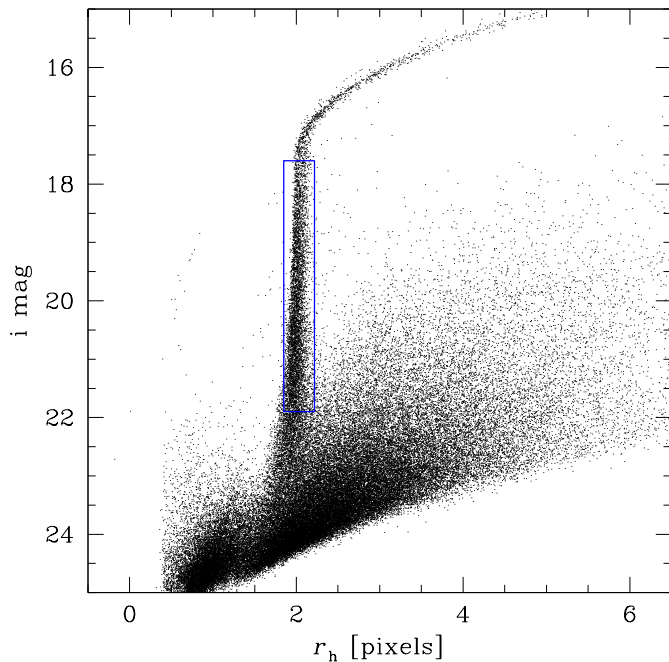
Fig. 5. Half-light-radius (r_h, estimated by SExtractor's FLUX_RADIUS) vs magnitude (MAG_AUTO) for a 520s CFHTLS exposure at high galactic latitude taken with the Megaprime instrument in the i band. The rectangle enclosing part of the stellar locus represents the approximate boundaries set automatically by PSFEx to select point-sources.

of $\sqrt{\chi^2}$ derived from the residual maps of point-sources is expected to be Gaussian to a good approximation. Contaminated profiles are identified using iterative $\kappa - \sigma$ clipping to the distribution of $\sqrt{\chi^2}$. Throughout our experiments, the value $\kappa = 4$ provided a consistent compromise between being too restrictive and being too permissive.
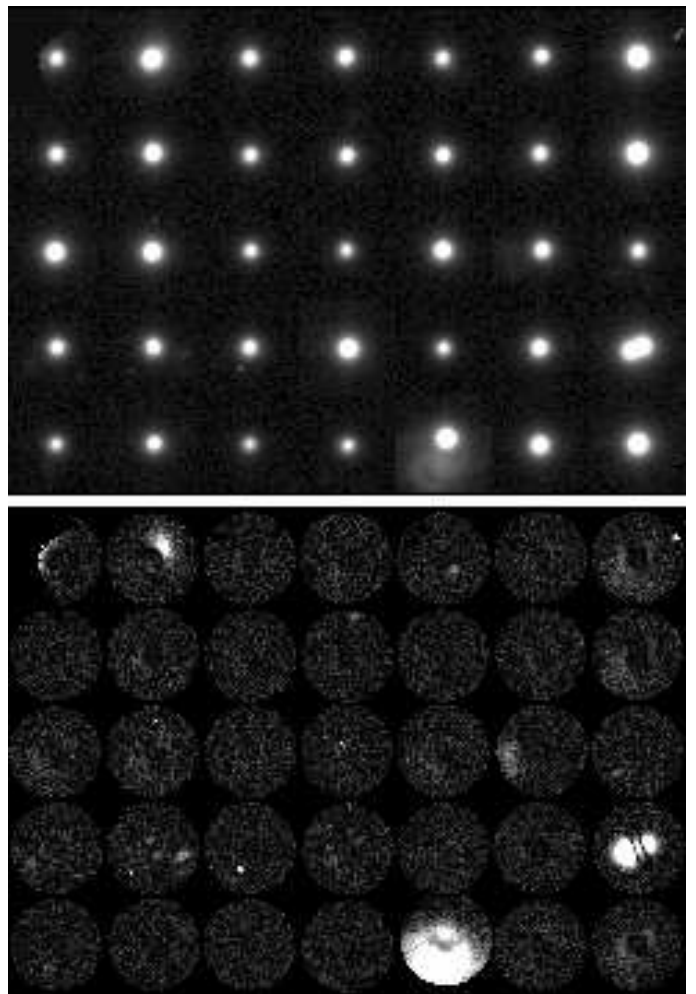
5. Quality assessment

Maintaining a certain level of image quality, and especially PSF quality, by identifying and rejecting "bad" exposures, is a critical issue in large imaging surveys. Image control must be automatized, not only because of the sheer quantity of data in modern digital surveys, but also to ensure an adequate level of consistency. Automatized PSF quality assessment is traditionally done based on point-source FWHM and ellipticity measurements. Although this is certainly efficient for finding fuzzy or elongated images, it cannot make the distinction between e.g. a defocused image and a moderately bad seeing.

In addition to the possibility to trace out the apparition of specific patterns using customized basis functions, PSFEx implements a series of generic quality measurements done on the PSF model as it varies across the field of view. The main set of measurements is done in PSF pixel space (oversampling factor η) by comparing the actual PSF model vector $\boldsymbol{\phi}$ with a reference PSF model $\rho(\boldsymbol{x'})$. We adopt as a reference model the elliptical Moffat (1969) function that fits best (in the chi-square sense) the model:

$$\rho(\boldsymbol{x'}) = I_0 \left(1 + \left\|A(\boldsymbol{x'} - \boldsymbol{x'_c})\right\|^2\right)^{-\beta}, \tag{15}$$

with

$$A = \frac{4}{\eta}(2^{-\frac{1}{\beta}} - 1) \begin{pmatrix} \cos\theta/W_{max} & \sin\theta/W_{max} \\ -\sin\theta/W_{min} & \cos\theta/W_{min} \end{pmatrix}, \tag{16}$$

Fig. 6. *Left*: some source images selected for deriving a PSF model of a MEGACAM image (the basic rejection tests based on SExtractor flags and measurements were voluntarily bypassed to increase the fraction of contaminants in this illustration). *Right*: map of residuals computed as explained in the text; bright pixels betray interlopers like cosmic ray hits and close neighbour sources.

where I_0 is the central intensity of the PSF, $\boldsymbol{x'_c}$ the central coordinates (in PSF pixels), W_{max}, the PSF FWHM along the major axis, W_{min} the FWHM along the minor axis, and θ the position angle (6 free parameters). As a matter of fact, the Moffat function provides a good fit to seeing-limited point-source images, and to a lesser degree, to the core of diffraction-limited images for instrument with circular apertures (Trujillo et al. 2001): in most imaging surveys, the "right" instrumental PSF will be very similar to a Moffat function with low ellipticity. Since PSFEx is meant to deal with significantly undersampled PSFs, another fit which we call "pixel-free" is also performed, where the Moffat model is convolved with a square top-hat function the width of a physical pixel, as an approximation to the real intra-pixel response function. The (non-linear) fits are performed using the LevMar implementation of the Levenberg-Marquardt algorithm (Lourakis 2004). They are repeated at regular intervals on a grid of PSF parameter vectors $\boldsymbol{a}$, generally composed of the image coordinates $\boldsymbol{x}$.

The average FWHM $(W_{max} + W_{min})/2$, ellipticity $(W_{max} - W_{min})/(W_{max} + W_{min})$ and β parameters derived from the fits pro-

vide a first set of local IQ estimators (Fig. 7). The second set is composed of the so-called *residuals* index

$$r = 2 \frac{\sum_i \left(\phi_i + \rho'(\boldsymbol{x}'_i) \right) \left| \phi_i - \rho'(\boldsymbol{x}'_i) \right|}{\sum_i \left(\phi_i + \rho'(\boldsymbol{x}'_i) \right)^2} \tag{17}$$

and the *asymmetry* index

$$\alpha = 2 \frac{\sum_i \left(\phi_i + \phi_{N-i} \right) \left| \phi_i - \phi_{N-i} \right|}{\sum_i \left(\phi_i + \phi_{N-i} \right)^2}, \tag{18}$$

where the ϕ_{N-i}'s are the point-symmetric counterparts to the ϕ_i components.

6. Use cases

6.1. Shear measurements

The quality of weak shear measurements critically depends on the mapping accuracy of PSF anisotropy. Earlier galaxy ellipticity recovery techniques would rely on the PSF's 2nd-order weighted moments only (Kaiser et al. 1995). More recent approaches require the full two-dimensional PSF model (Bernstein & Jarvis 2002, Refregier & Bacon 2003, Miller et al. 2007).

The absence of clearly visible residuals in PSF-subtracted, bright star images is a testimony to the global accuracy of models derived with PSFEx. But the modelling process features no constraint explicitly related to PSF ellipticity. We must therefore assess whether the derived models are usable for shear analyses at the bias level required by today's experiments (typically below the 0.1% level).

To this aim, we simulated 100 sets of realistic imaging data, each with a different (constant) PSF and random (constant) shear applied to 27 square degrees of (virtual) sky. The simulations include photon noise as well as source crowding and were generated using the STUFF[2] and SKYMAKER[3] software tools (Bertin 2009). Galaxies are simulated as a sum of a bulge component with de Vaucouleurs profile and an exponential disk. PSFs were extracted from a small sub-image with random size for every set, in order to check the influence of the number of stars used to model the PSF. Table 1 contains the main parameters used in the simulations, and the recovered PSFs are shown Fig. 8.
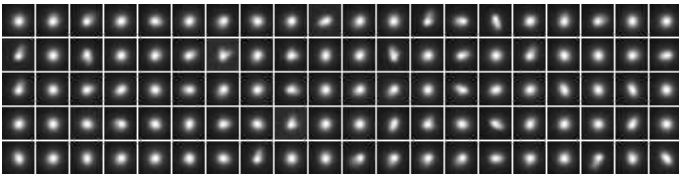
Fig. 8. PSFs simulated for shear testing and modelled using PSFEx.

Finally, average shear values were derived for each simulation set using the following typical, fully automated procedure:

1. Extract image sources in sub-images together with object pixel info with SEXTRACTOR;
2. Run PSFEx with default settings on the previously extracted catalogue to derive a (constant) PSF model;
3. Extract sources from the full simulations and fit 2-dimensional, PSF-convolved Sérsic models;

Table 1. Simulation parameters

Cosmology	$\Omega_m = 0.3$, $\Omega_\Lambda = 0.7$
Galaxy luminosity functions	Madgwick et al. (2003)
Galaxy luminosity+density evolution	Gabash et al. (2004)
Bulge sizes	Bingelli et al. (1984)
Disk sizes	de Jong & Lacey (2000)
Bulge apparent ellipticities	Sandage et al. (1970)
Disk apparent ellipticities	$\cos \theta$ with $-85° < \theta < +85°$
Shear $\gamma_{1/2}$	-0.05 – +0.05
Star and galaxy positions	Poissonian distribution
Star magnitude range	$17 - 26$
Star counts (expected)	$0.12 \, \text{dexp}(0.2 i_{AB}) \, \text{mag}^{-1} . \text{deg}^{-2}$
Photometric band	i (Megaprime)
Phot. zero-point ("ADUs, per sec.")	$i_{AB} = 25.72$ mag
Sky background	$\mu_{i_{AB}} = 20.4 \, \text{mag.arcsec}^{-2}$
Exposure time	12×300s
Pupil geom.	⌀3.6m primary, ⌀1m obscuration, '+'-shaped spider
Seeing (FWHM)	$0.1 - 0.8''$
Defocalisation (d_{80}[a])	$0.0 - 0.5''$
Astigmatism (d_{80}[a])	$0.0 - 0.6''$
Coma (d_{80}[a])	$0.0 - 0.6''$
Pixel scale	$0.186''$
Conversion factor	$1.6 \, \text{e}^-/\text{ADU}$
Readout noise	$5 \, \text{e}^-$

[a] diameter of the disk that contains 80% of the energy (ESO convention)

4. Average ellipticity components derived from the best-fitting Sérsic parameters of all unsaturated, uncropped galaxies with signal-to-noise ratio ≥ 20 (no weighting applied).

Step 3 is performed using a prototype version of SEXTRACTOR, that fits (in the χ^2 sense) Sérsic models convolved with the local PSF model. We measure a standard deviation of individual galaxy ellipticites $\sigma_1 = 0.205$. Since no weighting is applied to measurements, the standard error on ellipticities averaged for a set of N galaxies is therefore $\sigma_N = 0.205/\sqrt{N}$.

Concerns have recently been raised about the dangers of measuring shear parameters by fitting single Sérsic models to more complex galaxy profiles (Voigt & Bridle 2010). A small effect is indeed seen in our measurements, in the sense that shear amplitudes are over-estimated by about 1.5% (Fig. 9). This corresponds to a maximum difference of $\pm 7.10^{-4}$ in the measured shear with respect to the true value in our simulations. We corrected for this effect by dividing the ellipticity measurements by the slope in Fig. 9.

Figure 10 shows the shear residuals (measured shear with truth values subtracted) obtained for the 100 sets, as a function of various PSF characteristics. We observe that

– no significant trend is found with PSF ellipticity, despite the wide range of PSF shapes and aspect ratios (up to 2.3:1 !),
– no trend is found with PSF FWHM either, even for significantly undersampled images (FWHM < 2 pixels),
– constant PSFs do not seem to require a large number of stars as far as ellipticity measurements are concerned (some of the models here were derived with only 3 stars),
– there are hints of a small ellipticity bias ($\approx 1.10^{-3}$) for the most asymmetrical PSFs of the simulation ($\alpha > 0.2$). Hopefully, images with such extreme asymmetries are generally discarded from imaging surveys.

To this aim, we extracted the PSFs from the three sets of realisations generated by the week lensing community for the
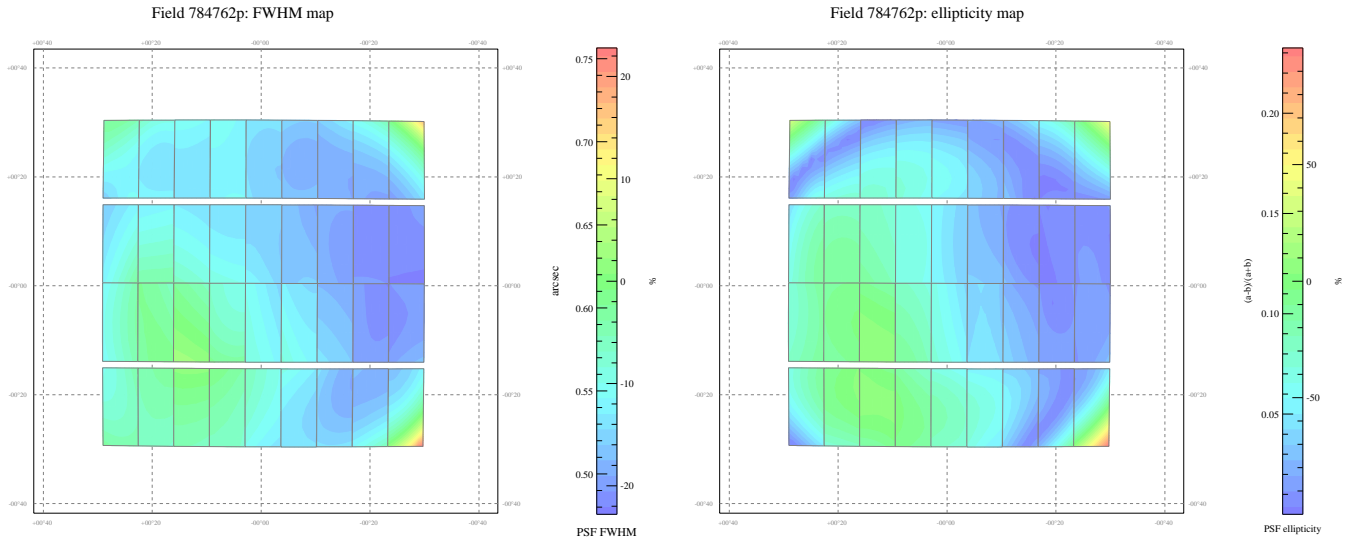
Fig. 7. Colour-coded maps of the PSF FWHM (left) and ellipticity (right) generated by PSFEx from a CFHTLS-Wide exposure The map and the individual Megaprime CCD footprints on the sky are presented in gnomonic projection (north is on top, east is on the left). PSF variations are modelled independently on each CCD using a 3rd degree polynomial (see text).
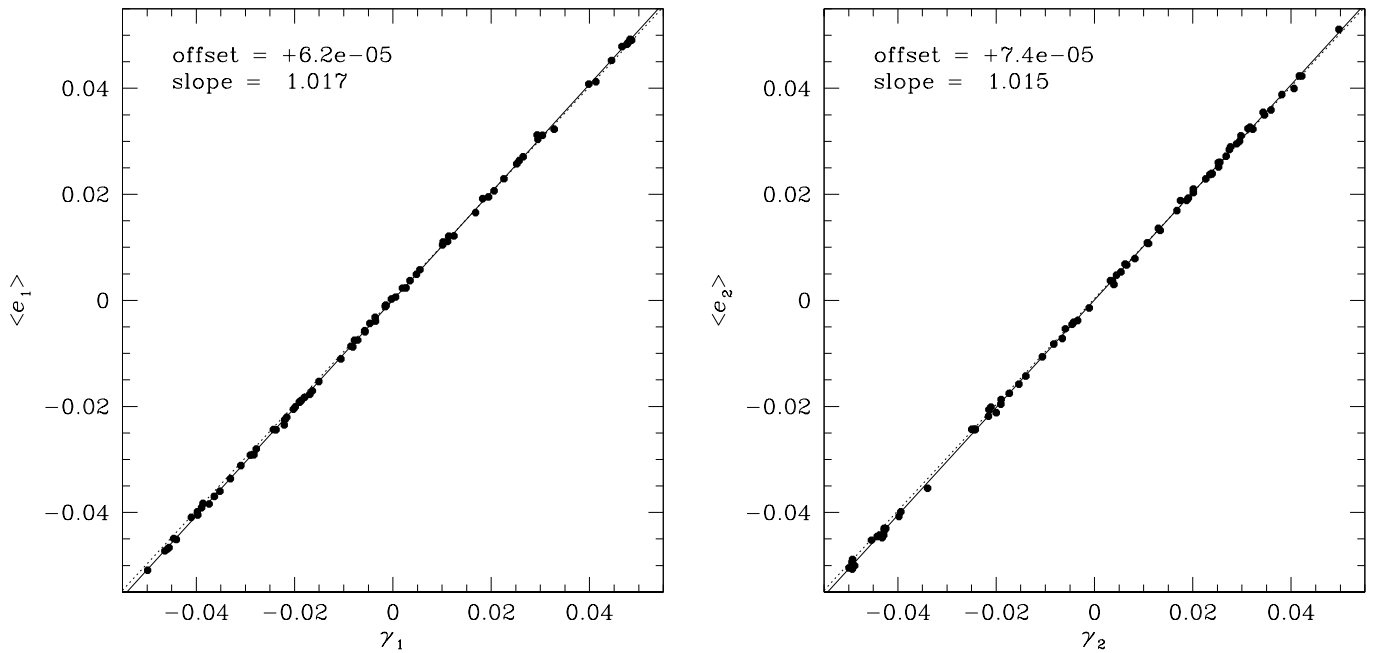
Fig. 9. Recovered averaged ellipticities $\langle e_{1,2} \rangle$ as a function of shear truth values $\gamma_{1,2}$.

Great'08 challenge (Bridle et al. 2009). As we are only interested in estimating the amount of biases in the modeling of the PSF, not in the measurement of

7. In practice

Building the normal equation matrix and solving the system (7) is fast: about 5 seconds for a 1000 pixel PSF and 100 stars on a 2GHz processor core.

8. Conclusion

1.

References

Alard C., Lupton R.H., 1998, ApJ, 503, 325
Anderson J., King I.R., 2000, PASP, 112,1360
Barron N., Borysow M., Beyerlein K., Brown M., Lorenzon W., Schubnell M., Tarlé G., Tomasch A., Weaverdyck C., 2007, PASP, 119, 466
Bendinelli O., Parmeggiani G., Piccioni A., Zavatti F., 1987, AJ, 94, 1095
Bernstein G.M., Jarvis M., 2002, AJ, 123, 583
Bernstein G., 2002, PASP, 114, 98
Bertin E., Arnouts S., 1996, A&AS, 117, 393
Bertin E., Mellier Y., Radovich M., Missonnier.G., Didelon P., Morin B., 2002, Astronomical Data Analysis Software and Systems XI, A.S.P. Conference
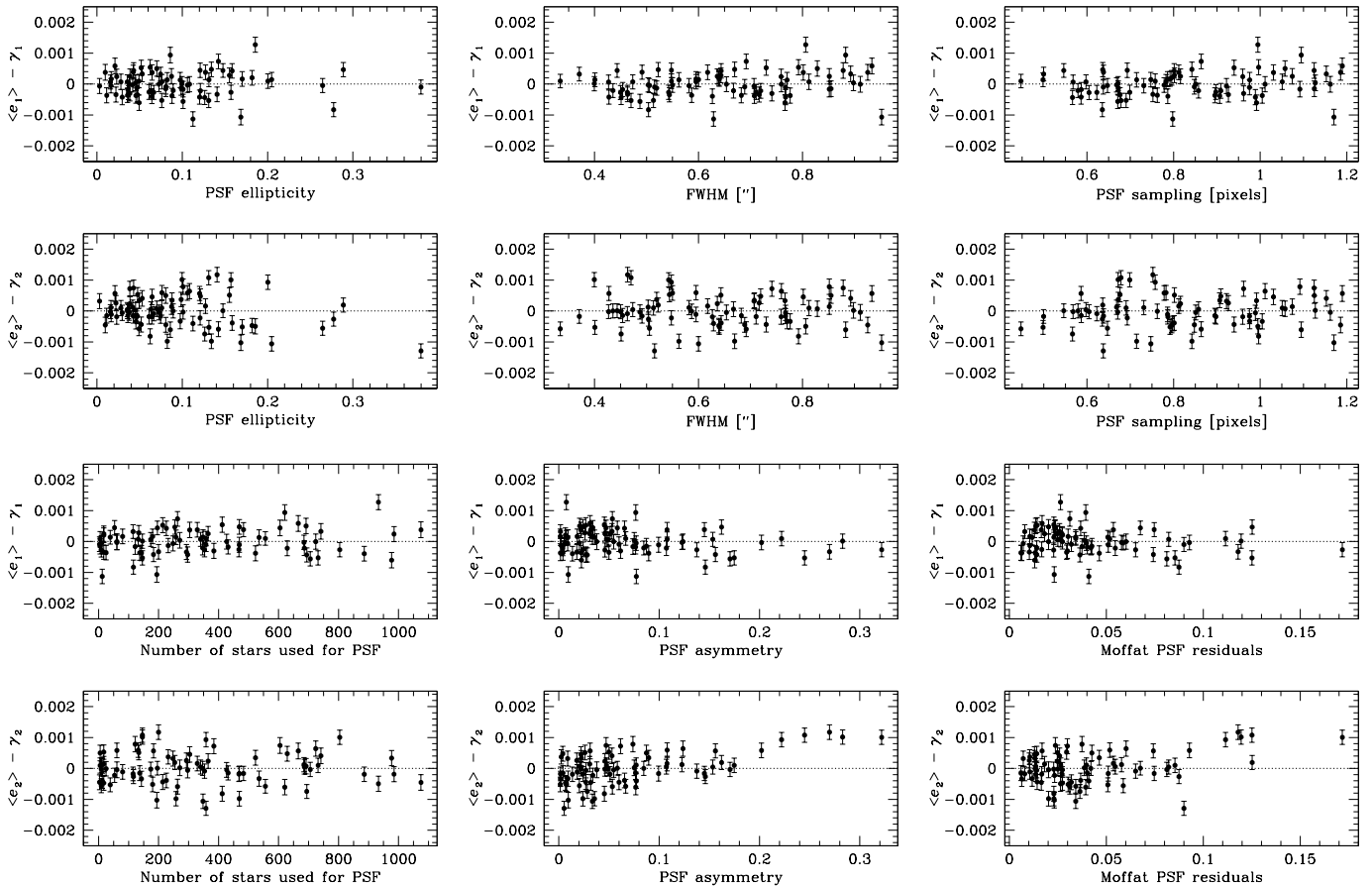
Fig. 10. Shear measurement residuals as a function of PSF characteristics. Error bars are 1σ formal estimates (see text).

Series, 281, 228

Bertin E., 2006, in Astronomical Data Analysis Software and Systems XV, A.S.P. Conference Series, 351, 112

Bertin E., 2009, in Mem. Soc. Astron. Ital., 80, 422

Binggeli B., Sandage A, Tarenghi M., 1984, AJ, 89, 64

Bridle S., Shawe-Taylor J. Amara A. Applegate D., Balan S.T., Bergé J., Bernstein G., Dahle H., Erben T., Gill M., Heavens A., Heymans C., High F.W., Hoekstra H., Jarvis M., Kirk D., Kitching T., Kneib J.-P., Kuijken K., Lagatutta D., Mandelbaum R., Massey R., Mellier Y., Moghaddam B., Moudden Y., Nakajima R., Paulin-Henriksson S., Pires S., Rassat A., Refregier A., Rhodes J., Schrabback T., Semboloni E., Shmakova M., van Waerbeke L., Witherick D., Voigt L., Wittman D., 2009, AnApS 3, 6

Buonanno R., Buscema G., Corsi C.E., Ferraro I., Iannicola G., 1983, A&A, 126, 278

Buonanno R., Iannicola G., 1989, PASP, 101, 294

de Jong R.S., Lacey C., 2000, ApJ, 545, 781

Delorme P., Willott C.J., Forveille T., Delfosse X., Reylé C., Bertin E., Albert L., Artigau E., Robin A., Allard F., Doyon R., Hill G., A&A, submitted

Diolaiti E., Bendinelli O., Bonaccini D., Close L., Currie D., Parmeggiani G., 2000, A&A, 147, 335

Franz O.G., 1973, JRASC, 67, 81

Gabasch A. Bender R., Seitz S., Hopp U., Saglia R. P. Feulner G., Snigula J., Drory N., Appenzeller I., Heidt J., Mehlert D. Noll S., Böhm A., Jäger K., Ziegler B., Fricke K. J., 2004, A&A, 421, 41

Gilliland R.L., Brown T.M., 1988, PASP, 100, 754

Hall P., Qiu P., 2007, The Annals of Statistics 35, 1512

Howell S.B., Koehn B., Bowell E., Hoffman M., 1996, AJ, 112, 1302

Huang T.S., Tsai R.Y., 1984, Advances in Computer Vision and Image Processing 1, 317

Jarvis M., Jain B., 2004, `arXiv:astro-ph/0412234v2`

Jee M.J., Blakeslee J.P., Sirianni M., Martel A.R., White R.L., Ford H.C., 2007, PASP, accepted

Kaiser N., Squires G., Broadhurst T., 1995, ApJ, 449, 460

Kalirai J.S., Richer H.B., Fahlman G.G., Cuillandre J.-C., Ventura P., D'Antona F., Bertin E., Marconi G., Durrell P.R., 2001a, AJ, 122, 257

Kalirai J.S., Richer H.B., Fahlman G.G., Cuillandre J.-C., Ventura P., D'Antona F., Bertin E., Marconi G., Durrell P.R., 2001b, AJ, 122, 266

Kendall T.R., Bouvier J., Moraux E., James D.J., Ménard F., 2005, A&A,

Krist J.E., 2004, SPIE, 5499, 328

Lauer T.R., 1999, PASP, 111, 1434

Lauer T.R., 1999, PASP, 111, 227

Lodieu N., Bouvier J., James D.J., de Wit W.J., Palla F., McCaughrean M.J., Cuillandre J.-C., 2006, A&A, 450, 147

Lourakis M.I.A., 2004, `http://www.ics.forth.gr/~lourakis/levmar`

Lupton R.H., Gunn J.E., 1986, AJ, 91, 1106

Lupton R., Gunn J.E., Ivezić Z., Knapp G.R., Kent S., 2001, in Astronomical Data Analysis Software and Systems X, A.S.P. Conference Series, 238, 269

Luxen M., Förstner W., 2002, Proceedings of the PCV'02 Symposium, 205

Madgwick D.S., Lahav O., Baldry I. K., Baugh C. M., Bland-Hawthorn J., Bridges T., Cannon R., Cole S., Colless M., Collins C., Couch W., Dalton G., De Propris R., Driver S. P., Efstathiou G., Ellis R. S., Frenk C. S., Glazebrook K., Jackson C., Lewis I., Lumsden S., Maddox S., Norberg P., Peacock J. A., Peterson B. A., Sutherland W., Taylor K., 2002, MNRAS, 333,133

Magain P., Courbin F., Gillon M., Sohy S., Letawe G., Chantry V., Letawe Y., 2007, A&A, 461, 373

Martens J.-B., 1990, IEEE Transactions Acoustics, Speech, Signal Processing 38, 1607

Martens J.-B., 2006, EURASIP Journal on Applied Signal Processing vol. 2006, 1

Massey R., Refregier A., 2005, MNRAS, 363, 197

Mighell K.J., 2005, MNRAS, 361, 861

Miller L., Kitching T.D., Heymans C., Heavens A.F., van Waerbeke L., 2007, MNRAS, 382, 315

Moffat A.F.J., 1969, A&A, 3, 455

Moraux E., Bouvier J., Stauffer J.R., Cuillandre J.-C., 2003, A&A, 400, 891

Penny A.J., Leese R., 1996, in Astronomical Data Analysis Software and Systems V, A.S.P. Conference Series, 101, 29

Penny A.J., 1979, MNRAS, 187, 829

Pinheiro da Silva L., Auvergne M., Toublanc D., Rowe J., Kuschnig R., Matthews J., 2006, A&A, 452, 363

Racine R., 1996, PASP, 108, 699

Refregier A., 2003, MNRAS, 338,35

Refreguier A., Bacon D., 2003, MNRAS, 338, 48

Roddier F., 1981, Prog. Optics, 19, 281

Sandage A., Freeman K.C., Stokes N.R., 1970, ApJ, 160, 831

Schechter P.L., Mateo M., Saha A., 1993, PASP, 105, 1342

Sérsic J.L., 1968, Atlas de Galaxias Australes, Observatorio Astronomico, Cordoba

Stetson P.B., 1987, PASP, 99, 191

Theodoridis S., Koutroumbas K., 2003, Pattern Recognition (second edition), Academic Press, 212

Toyozumi H., 2005, PhD dissertation, The University of New South Wales

Trujillo I., Aguerri J.A.L.,Cepa J., Gutiérrez C.M., 2001, MNRAS, 328, 977

Voigt L.M., Bridle S.-L., 2010, MNRAS, 404, 458

Wolberg G., 1992, Digital Image Warping, IEEE Computer Society Press